# Experimental characterization of spin-$\frac{3}{2}$ silicon vacancy centers in 6*H*-SiC

Harpreet Singh,[1,*] Andrei N. Anisimov,[2] Sergei S. Nagalyuk,[2] Eugenii N. Mokhov,[2] Pavel G. Baranov,[2] and Dieter Suter[1]

[1]*Fakultät Physik, Technische Universität Dortmund, D-44221 Dortmund, Germany*

[2]*Ioffe Institute, St. Petersburg 194021, Russia*

(Received 19 January 2020; revised manuscript received 14 March 2020; accepted 2 April 2020; published 27 April 2020)

Silicon carbide (SiC) hosts many interesting defects that can potentially serve as qubits for a range of advanced quantum technologies. Some of them have very interesting properties, making them potentially useful, e.g., as interfaces between stationary and flying qubits. Here we present a detailed overview of the relevant properties of the spins in silicon vacancies of the 6*H*-SiC polytype. This includes the temperature-dependent photoluminescence, optically detected magnetic resonance, and the relaxation times of the longitudinal and transverse components of the spins during free precession as well as under the influence of different refocusing schemes.

DOI: 10.1103/PhysRevB.101.134110

## I. INTRODUCTION

### A. Spin centers in silicon carbide

Silicon carbide (SiC) is known for the diversity of its polytypes with remarkable and tunable electrical and optical properties as well as its radiation stability [1,2]. SiC has a large band gap with deep defects and is supported by sophisticated fabrication techniques [3–6]. Recently, silicon vacancy ($V_{Si}$) centers in SiC were proposed as an alternative to nitrogen vacancy (NV) centers in diamond for spintronics and quantum technologies [7]. The photoluminescence of the defects in SiC lies in the near infrared, which allows, e.g., optical detection of spin states [8–12]. The color centers in SiC can be grouped into two classes depending on their spin in the ground state: $S = 1$ or $S = 3/2$ [1,9,13–18]. The divacancies ($V_{Si} - V_C$) are formed by adjacent pairs of Si and C vacancies, have spin $S = 1$, and are known as P6 and P7 in the literature [8,9,19–21].

The four dangling $sp^3$ orbitals at the $V_{Si}$ site contribute four electrons. If $V_{Si}$ captures an additional electron, then it becomes a negatively charged silicon vacancy ($V_{Si}^-$) [16,22–24] whose spin state was shown to be $S = 3/2$ by a radiofrequency-optical double resonance technique [23,25]. The site symmetry of $V_{Si}^-$ is $C_{3v}$, as shown in Fig. 1. Several separately addressable $V_{Si}^-$ have been identified in the same crystal for each of the main SiC polytypes: hexagonal 4*H*-SiC and 6*H*-SiC and rhombic 15R-SiC. The 4*H*-SiC polytype, e.g., hosts one hexagonal ($h$) and one cubic ($k$) lattice site and in 6*H*-SiC there are one hexagonal and two cubic sites ($h$, $k_1$, and $k_2$). $V_{Si}^-$ at a hexagonal site $h$ of 4*H*- and 6*H*-SiC is called a $V_2$ type vacancy, at a cubic site $k$ of 4*H*-SiC it is called $V_1$ and in 6*H*-SiC $V_1$ and $V_3$ are located at sites $k_1$ and $k_2$ [13].

The spins of $V_{Si}^-$ in SiC are highly controllable and can be manipulated with the techniques that have been developed, e.g., for working with diamond NV qubits. This was demonstrated with ensembles [26] as well as with single centers [7]. Optically induced spin polarization of the ground state at room temperature has been demonstrated using electron spin resonance [27]. This spin polarization can be used to implement solid-state masers and extraordinarily sensitive radio-frequency amplifiers [10] or magnetic field sensors with dc field sensitivities $>100$ nT/$\sqrt{\text{Hz}}$ [28]. In some $V_{Si}^-$ the zero-field splitting (ZFS) is nearly temperature independent, making these centers very attractive for vector magnetometry. Contrarily, the zero-field splitting of the centers $V_2$ centers in 4*H*-SiC in the excited state exhibits a large thermal shift, which makes them useful for thermometry applications [29]. All four ground-state spin levels of $V_{Si}^-$ have been used to demonstrate absolute dc magnetometry, which is immune to thermal noise and strain inhomogeneity [30].

### B. Preserving spin coherence

An important precondition for the implementation of quantum technologies, including quantum information processing is that the phase of superposition states can be preserved for times significantly longer than the duration of the computational task [31,32]. Achieving this goal generally requires an array of measures [33], including passive schemes like decoherence-free subspaces [34] or active schemes like spin-echoes [35]. In divacancy spin ensembles in 4*H*-SiC, Hahn-echo times longer than 1 ms were observed at 20 K [20].

In most cases, the interactions with the environment that cause the dephasing are not static and a single refocusing pulse is not sufficient to completely suppress the dephasing. For those cases, multiple echo sequence were developed by Carr and Purcell [36], consisting of equidistant $\pi$ pulses. This basic experiment was improved to make it more robust with respect to experimental imperfections [37–39]. These so-called dynamical decoupling (DD) techniques have been applied to extend the coherence times of different types of

*harpreet.singh@tu-dortmund.de

 

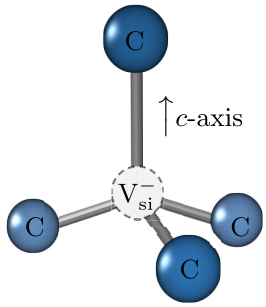


FIG. 1. Structure of a negatively charged spin 3/2 silicon-vacancy ($V_{Si}^-$). The blue spheres with labels C represent the carbon atoms. The white circle with the dashed boundary represents the $V_{Si}^-$.

qubits, including, e.g., rare-earth ions [40] and the spin of the NV center in diamonds [41]. In the $V_2$ vacancy of the 4*H*-SiC polytype, the efficiency of the spin-echo experiment depends strongly on the magnetic field [42]. Combining Carr-Purcell-Meiboom-Gill (CPMG) decoupling with a static magnetic field can extend the spin coherence time of the $V_2$ center in 4*H*-SiC to more than 20 ms [43].

### C. Outline of this paper

In this work, we focus on the 6*H*-SiC polytype whose spin properties have not yet been studied in detail. Section II gives details of the sample preparation, photoluminescence measurement, and the optical pumping scheme. Section III describes the experimental setup for continuous-wave as well as pulsed optically detected magnetic resonance (ODMR) measurements. Section IV describes the results of the spin-lattice and spin-spin relaxation measurements. Section V contains the discussion and concluding remarks.

## II. SYSTEM

### A. Sample

The experiments were performed on a sample that was isotopically enriched in $^{28}$Si and $^{13}$C. The Si enrichment was performed using gas-centrifuge technology, resulting in an isotopic purity of 99.999%, which was available in the form of small $^{28}$Si pieces (1–3 mm). The $^{13}$C source was carbon powder enriched to 15% in $^{13}$C. The SiC crystal was grown at a temperature of 2300°–2400°C on a (0001) Si face in an argon atmosphere at a growth rate of ≈100 $\mu$m/h. After growing the SiC crystal, machining and cutting of the wafers were carried out. The isotope composition was measured by secondary ion mass spectroscopy (SIMS). The concentrations of $^{28}$Si, $^{29}$Si, and $^{30}$Si are 99.918, 0.076, and 0.006%, respectively. The concentrations of $^{12}$C and $^{13}$C are 95.3 and 4.7%, respectively. To create $V_{Si}^-$ centers, the crystal was irradiated with electrons with a dose of $10^{18}$ cm$^{-2}$ and an energy of 2 MeV at room temperature.

### B. Photoluminescence

To measure the photoluminescence (PL) of the sample, we used the setup shown schematically in Fig. 2. A Ti:sapphire laser provided the optical excitation. The PL was collected

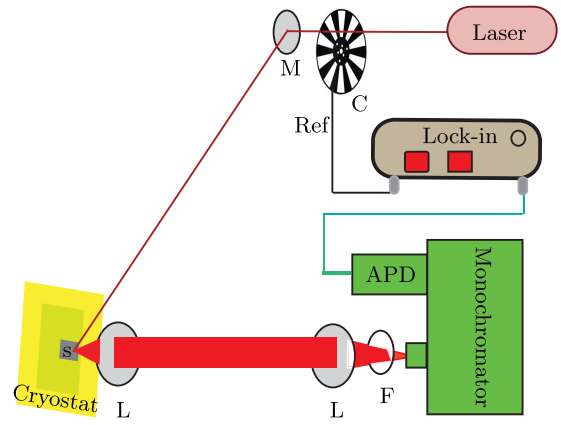


FIG. 2. Experimental setup for photoluminescence measurements. The red line from the laser represents the laser beam and C denotes the mechanical chopper. The gray rectangle labeled S is the SiC sample. Ellipsoids labeled M, L, and F represent reflecting mirrors, convex lenses, and a long-pass filter, respectively. The rectangle labeled APD represents the avalanche photodiode module.

with the help of two convex lenses of focal length 20 cm. The PL was collected in the direction of the *c* axis and passed through a long-pass 850-nm filter (F; Thorlabs) to a monochromator (Spex 1704). An avalanche photodiode (APD) module with a frequency bandwidth from dc to 100 kHz (C5460-1 series from Hamamatsu) was attached to the monochromator for detecting the PL. The voltage output of this APD was measured with the lock-in amplifier (SRS model SR830). The laser beam was modulated with a chopper, whose sync signal served as reference for the lock-in amplifier.

Figure 3 shows some PL spectra recorded at different temperatures with the excitation laser set to 790 nm. The sample was cooled down using a helium cryostat, and the PL spectra recorded at ≈5.4 K, 150 K, 200 K, 250 K, and 300 K are shown. The zero phonon lines (ZPL) of the negatively

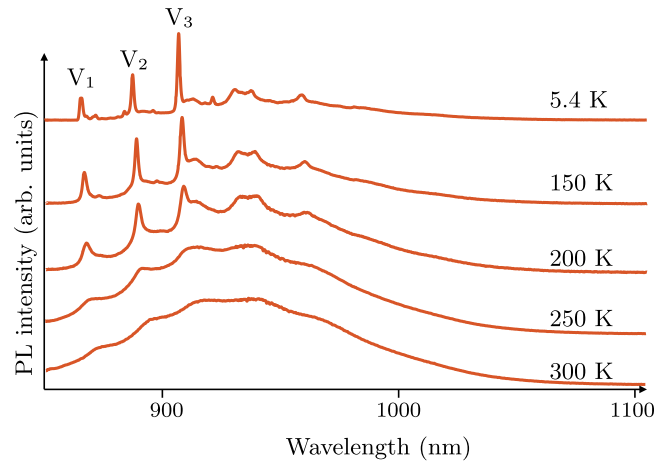


FIG. 3. PL spectra measured at different temperatures. The sample is excited with a 790-nm laser. Peaks labeled $V_1$, $V_2$, and $V_3$ correspond to the zero-phonon lines of $V_{Si}^-$ at the lattice sites $k_1$, $h$, and $k_2$, respectively.

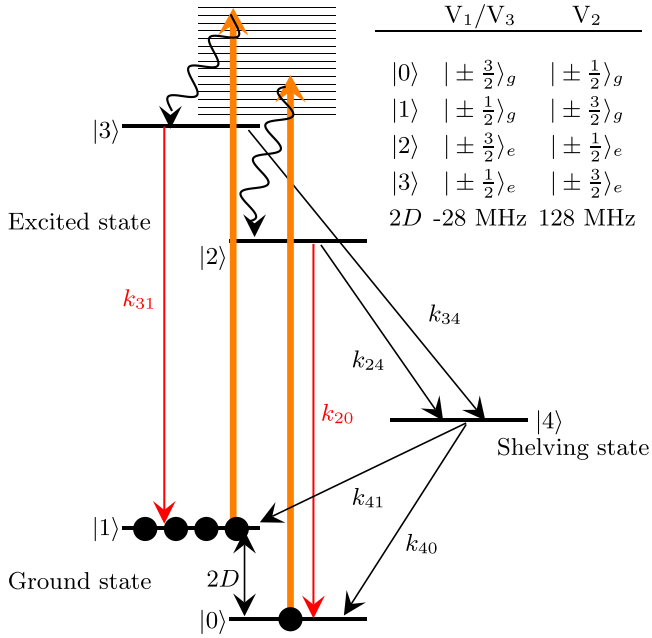


FIG. 4. Energy-level diagram of the 6*H*-SiC $V_{Si}^-$ showing the ground, excited, and shelving states. Radiative transitions with rates $k_{31}$ and $k_{20}$ are marked by red arrows. The laser beam excitation is shown with thick orange arrows. Spin-dependent nonradiative transitions generating the ground-state spin polarization are shown as black arrows. States $|0\rangle$ and $|1\rangle$ represent the degenerate $|\pm\frac{3}{2}\rangle$ ($|\pm\frac{1}{2}\rangle$) and $|\pm\frac{1}{2}\rangle$ ($|\pm\frac{3}{2}\rangle$) ground states of the $V_1/V_3$ ($V_2$) type $V_{Si}^-$. The states $|2\rangle$ and $|3\rangle$ represent the doubly degenerate excited states and $|4\rangle$ the shelving states.

charged vacancies are visible at the expected wavelengths of 865 nm ($V_1$), 887 nm ($V_2$), and 908 nm ($V_3$) [13,44].

### C. Energy levels and optical pumping

The negatively charged defects in 6*H*-SiC have spin $S = 3/2$ [23,25]. Figure 4 shows the energy-level diagram of the 6*H*-SiC $V_{Si}^-$ in the absence of an external magnetic field. The states $|0\rangle$ and $|1\rangle$ in the electronic ground state correspond to the $S = 3/2$ $m_S = \pm\frac{3}{2}$ and $\pm\frac{1}{2}$ spin states. In the absence of a magnetic field, they form two degenerate doublets, which are split by the zero-field interaction. In the case of the $V_1/V_3$ vacancy, the $m_S = \pm\frac{3}{2}$ are lower in energy, i.e., they correspond to state $|0\rangle$, in the $V_2$ vacancy, the $\pm\frac{1}{2}$ states are the lowest energy states [10,45]. The states $|2\rangle$ and $|3\rangle$ represent the $S = 3/2$, $m_S = \pm\frac{3}{2}(\pm\frac{1}{2})$, and $\pm\frac{1}{2}$ $(\pm\frac{3}{2})$ spin substates of the electronically excited states of $V_1/V_3$ ($V_2$) [11,12]. The shelving state $|4\rangle$ is an $S = 1/2$ state, which is important for the optical pumping process [11].

The spin Hamiltonian of the $S = 3/2$ states is

$$\mathcal{H} = D\left(S_z^2 - 5/4\right) + g\mu_B \vec{B}\cdot\vec{S}, \qquad (1)$$

where the zero field splitting in the electronic ground state is $2D = -28$ MHz for $V_1/V_3$ and 128 MHz for $V_2$ [45], $g = 2.0$ is the electron $g$ factor, $\mu_B$ is the Bohr magneton, $\vec{B}$ is the external magnetic field, and $S$ is the vector of the electron spin operators. We use a coordinate system whose $z$ axis is oriented along the $C_3$ symmetry axis, which is also

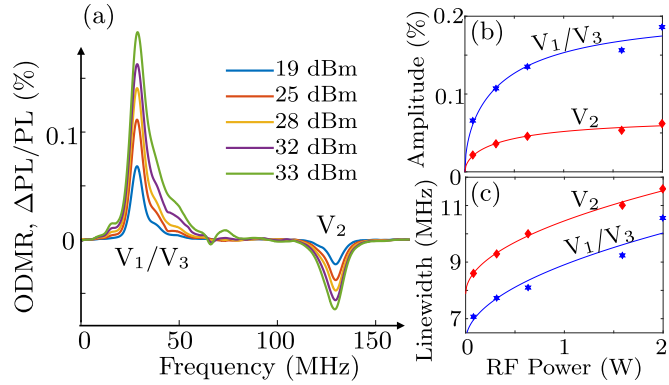


FIG. 5. (a) ODMR signal vs frequency recorded with different RF powers in zero magnetic field. The horizontal axis is the frequency in MHz and the vertical axis the relative change of the PL, recorded by the lock-in amplifier. (b) ODMR signal vs RF power and (c) linewidth vs RF power.

the $c$ axis. In the absence of optical pumping, when the spin system is in thermal equilibrium at room temperature, all four ground states are almost equally populated. When the system is irradiated with a laser, the populations are redistributed, as shown schematically in Fig. 4. When the laser is turned on, it excites transitions from the ground states $|0\rangle$ and $|1\rangle$ to the excited states $|2\rangle$ and $|3\rangle$. From the excited states $|2\rangle$ and $|3\rangle$ most of the population falls back to the $|0\rangle$ and $|1\rangle$ states by spontaneous emission with a rate $k_{20}$ and $k_{31}$. However, the system can also undergo intersystem crossing (ISC) to the shelving states $|4\rangle$ with the rates $k_{24}$ and $k_{34}$ [11]. From there the system returns to the ground state, with a bias for the state $|1\rangle$ over state $|0\rangle$ with the rates $k_{40}$ and $k_{41}$ [25,30,45]. The exact ISC rates from and to the shelving state are not yet known precisely but, by considering the recorded ODMR data shown in Fig. 5, $k_{34} > k_{24}$ for $V_1/V_3$ and $k_{24} > k_{34}$ for $V_2$.

## III. OPTICALLY DETECTED MAGNETIC RESONANCE

### A. Continuous-wave ODMR

To determine the ground-state spin Hamiltonian of the $V_{Si}^-$ in the sample, we used the continuous-wave (cw) ODMR technique with the setup shown in Fig. 6. Our light source was a 785-nm laser diode with a maximum power of 400 mW, which was driven by a Thorlabs laser diode controller (LDC202C series) with a thermoelectric temperature controller (TED 200°C). We used three orthogonal Helmholtz coil-pairs for applying the static magnetic field in an arbitrary direction. A highly stable linear current source (Servowatt, three-channel DCP-390/30) delivers currents up to 15 A to the coils. The currents were controlled individually by an analog control voltage. The radio-frequency (RF) signal was generated with a direct digital synthesizer (DDS) AD9915 from Analog Devices which generates signals up to 1 GHz. Its output was amplified using an RF amplifier (Mini- Circuit LZY-1, 50W amplifier with a frequency range from 20 to 512 MHz) and sent to a 50-$\mu$m wire terminated with a 50-Ω resistor. A programmable function generator (PFG, Hameg model HM8130-2) was used to modulate the amplitude of the RF field. A laser beam was focused on the sample using

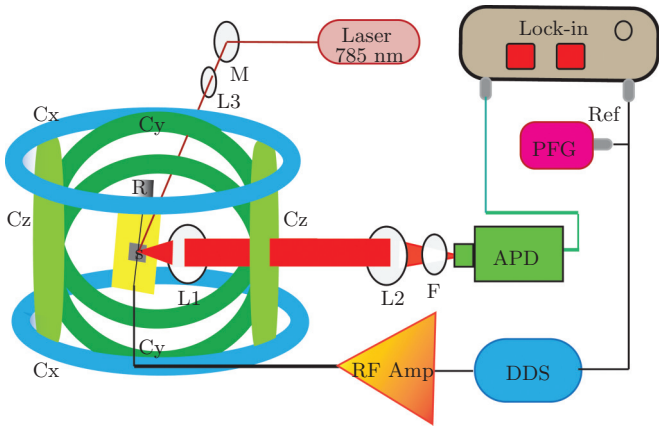


FIG. 6. Experimental setup for measuring the ODMR of silicon vacancies. The red line from the laser represents the path of the laser beam. Ellipsoids labeled M, L, and F represent mirrors, convex lenses, and long-pass filter, receptively. The gray rectangle labeled with S is the SiC sample. The RF is applied using straight a 50 $\mu$m diameter copper wire placed over the sample, in series with a 50-Ω resistor which is represented by a rectangle labeled with R. The tree orthogonal ring-pairs Cx, Cy, and Cz represent Helmholtz coils. They allows us to apply magnetic fields in an arbitrary direction. Rounded rectangles labeled PFG, APD, and DDS represent a programmable function generator, an avalanche photodetector module and a direct digital synthesizer, respectively.

a convex lens (L3) of focal length 20 cm. The PL from the sample was collected with a pair of lenses (L1 and L2 with focal lengths 5 and 15 cm, respectively), sent through a 850-nm long-pass filter to suppress stray light from the laser and to an avalanche photodiode (APD) module with a frequency range from dc to 10 MHz (C12703 series from Hamamatsu). The APD signal was demodulated with a lock-in amplifier (SRS model SR830 DSP) whose reference signal was derived from the PFG modulating the RF.

Figure 5(a) shows the ODMR signal recorded in the absence of a magnetic field by sweeping the frequency of the RF at different RF powers, using the setup shown in Fig. 6. Two peaks with different signs are observed: a positive one (i.e., increase of PL at the application of RF) at 28 MHz and a negative one at 128 MHz. In a previous work [13], it was shown that the peak at 128 MHz corresponds to the $V_{Si}^-$ at lattice sites $h$ ($V_2$ type) and the peak at 28 MHz corresponds to $V_{Si}^-$ at two quasicubic sites $k_1$ and $k_2$ ($V_1$ and $V_3$ type) which have the same $D$ value [13]. Recently it has been shown the peak at 28 MHz corresponds to $V_{Si}^-$ at quasicubic site $k_1$ and the peak at 128 MHz corresponds to the $V_{Si}^-$ at the quasicubic site $k_2$ ($V_3$ type) [45]. Since the ODMR peaks assignment is still debatable, we will follow the ODMR peaks assignment used in earlier work [13].

The overall ODMR contrast is relatively small, but comparable to the values from similar systems (see, e.g., Refs. [10,29,30,43]). While not all the relevant parameters are known, one reason for the relatively small contrast is that the PL from the different types of vacancies can not be separated at room temperature, as shown in Fig. 3. The measured PL therefore includes baseline contributions from other centers that do not depend on the magnetic resonance.

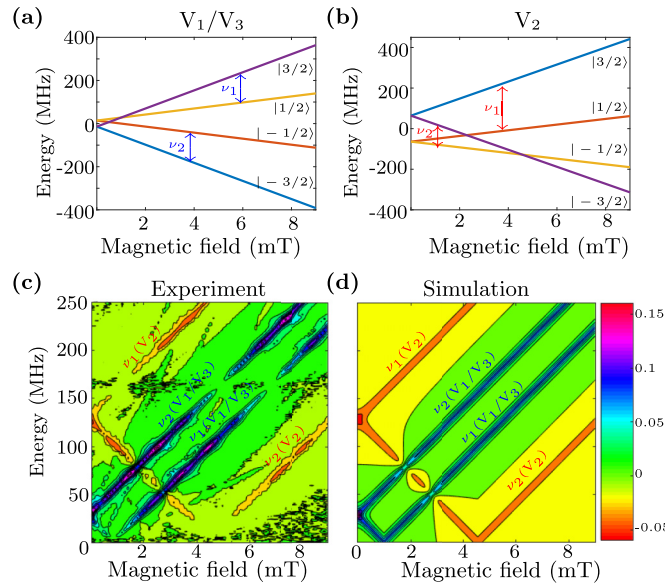


FIG. 7. Energy levels of (a) the $V_1/V_3$ vacancy and (b) $V_2$ vacancy in a magnetic field $B \parallel c$ axis. (c) Experimental ODMR and (d) simulated ODMR showing resonances from $V_1/V_3$ and $V_2$ for a range of magnetic fields $B \parallel c$ axis. The color scale in (c) and (d) is in units of $\Delta PL/PL\%$.

The variation of amplitude and linewidth with RF power is shown in Figs. 5(b) and 5(c), respectively. The amplitude data were fitted with the function

$$S(P) = S_{\max}[P/(P_0 + P)],$$

where $S(P)$ is the signal amplitude and $P$ the RF power. $S_{\max}$ and $P_0$ are the fitting parameters and the resulting values were 0.2087% and 0.8573 $W$ (0.07112% and 0.8834 $W$) for $V_1/V_3$ ($V_2$), respectively. The linewidth data were fitted to the function

$$LW(P) = LW_0 + a\sqrt{P},$$

where $LW(P)$ is the linewidth. The resulting values for the fitting parameters $LW_0$ and $a$ were 6.193 MHz and 2.713 MHz $W^{-1/2}$ (7.877 MHz and 2.579 MHz $W^{-1/2}$) for $V_1/V_3$ ($V_2$) respectively. At the maximum RF power that we could apply, 33 dBm, the ODMR signal $\Delta PL/PL$ reached an amplitude of 0.19 % (−0.06 %) for $V_1/V_3$ ($V_2$) and the linewidth of $V_1/V_3$ ($V_2$) was 10.24 MHz (11.70 MHz).

Figures 7(a) and 7(b) shows the energy levels of $V_1/V_3$ and $V_2$ as a function of the magnetic field $B$ applied $\parallel$ $c$ axis, calculated from the Hamiltonian given in Eq. (1). Arrows labeled with $\nu_1$ and $\nu_2$ represent the transition from $|3/2\rangle \longleftrightarrow |1/2\rangle$ and $|-3/2\rangle \longleftrightarrow |-1/2\rangle$ respectively. Figure 7(c) summarizes the ODMR spectra for a range of magnetic fields from 0 to 9 mT, applied parallel to the $c$ axis, using an RF power of 32 dBm (1.6 W). In this plot the magnetic field strength $B$ is plotted along the horizontal axis and the vertical axis corresponds to the RF frequency. The relative change of the PL is color-coded as shown by the color bar to the right of the plot. For frequencies <20 MHz, the RF power generated by the available amplifier drops significantly, which leads to the very small ODMR signal in this range. Also, at a frequency of

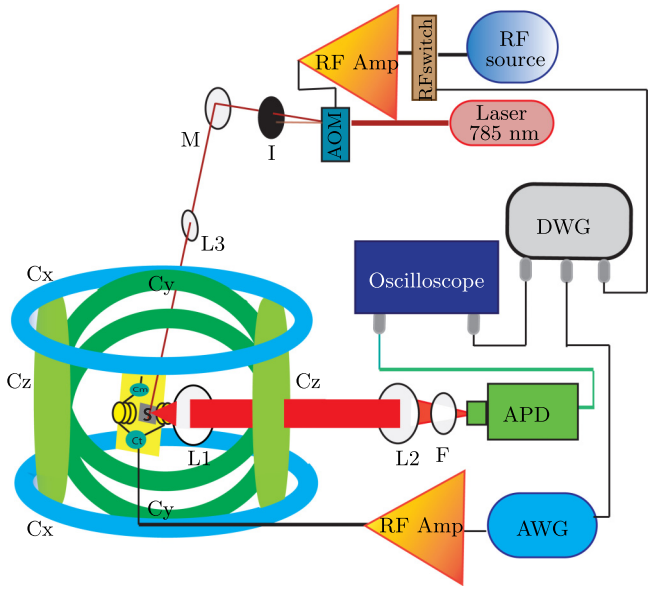


FIG. 8. Experimental setup used for measuring the relaxation rates. The acousto-optical modulator (AOM) generates the laser pulses. The red line from the laser represents the path of the laser beam. Ellipsoids labeled with M, L, and F represent reflecting mirrors, convex lenses, and long-pass filter, receptively. DWG is a digital word generator (TTL pulse generator). The gray rectangle labeled with S is the SiC sample. AWG is an arbitrary waveform generator. The RF is applied to the sample by a resonant LC circuit.

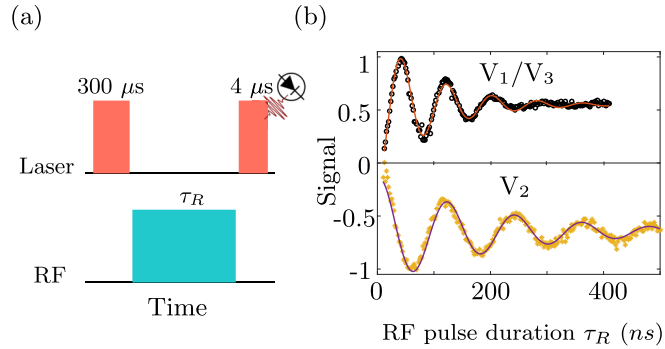


FIG. 9. (a) Pulse sequence for measuring Rabi oscillations. The red and blue rectangles represent the laser and RF pulses and the pulse duration is written above the pulse. (b) Experimental Rabi oscillations for $V_1/V_3$ and $V_2$. The $y$ axis represents the normalized change of the PL signal and the $x$ axis the RF pulse duration $\tau_R$.

~165 MHz, we observed very small signals, which appears to be do to a standing wave in our RF system, which was not impedance-matched to the 50 Ω amplifier. The experimental data compare well to the superposition of the signals from the two types of Si vacancies, which is shown in Fig. 7(d). For this simulation, the transition frequencies are obtained from the Hamiltonian of Eq. (1), while amplitudes and linewidths are taken from the experimental data.

### B. Pulsed ODMR

The uncontrolled interaction with a noisy environment has two effects on a system that has been excited from its thermal equilibrium state: It causes dephasing and a return of the system to the thermal equilibrium state. If the system is used in quantum technology applications [32,46], both effects are unwanted since long coherence times are an essential requirement for technologies like quantum computing, quantum metrology and quantum memories. To assess the suitability of for these applications, a precise characterisation of the decoherence processes is therefore essential. For this purpose, we use the time-resolved ODMR technique [47,48].

For the time-resolved measurements, we modified the setup of Fig. 6 to generate laser- and RF pulses of variable duration. Figure 8 shows the modified setup. For generating the laser pulses, we used an acousto-optical modulator (AOM; NEC model OD8813A). The center frequency of the AOM was 100 MHz, and the RF power was 1.2 W. The RF control signal was generated by a programmable 1-GHz synthesizer HM8133-2 and the RF pulses were generated by an RF switch (Mini-Circuits ZASWA-2-50DR+, dc-5 GHz). The TTL pulses that control the timing were generated by a SpinCore PulseBlaster ESR-PRO PCI card. The RF pulses that drive the spins were generated by an AWG (WavePond, Chase Scientific, DAx14000). The RF pulses were amplified up to 50 W and applied to the SiC sample through a tuned circuit for minimizing reflections. The signal from the APD detector was recorded with a USB card (PicoScope 2000 series) attached to a computer.

In all experiments described below, a laser pulse of 75-mW power and 300-$\mu$s duration initializes the SiC vacancies by populating the state $|1\rangle$ more than the state $|0\rangle$. At this laser intensity, the time constant for the transfer of population to spin state $|1\rangle$ is 28 $\mu$s (11 $\mu$s) for $V_2$ ($V_1/V_3$). After the polarization of the spin system, a sequence of RF pulses was applied to the system, as discussed in detail below. To read out the final state of the spin system, we applied a second laser pulse of duration 4 $\mu$s during which we collect the PL as described in Sec. III A. In the time-resolved experiment, we averaged the signal 500 times and subtracted it from a 500 times averaged signal of a reference pulse sequence to remove unwanted background signals. This process was repeated 5 times and again the average was taken.

To calibrate the strength of the RF field for the pulsed excitation, we performed a measurement of Rabi oscillations for the transition between the $|0\rangle$ and $|1\rangle$ of $V_{\mathrm{Si}}^-$, using the pulse sequence shown in Fig. 9(a). After this initializing laser pulse, a 16 W RF pulse of variable duration $\tau_R$ was applied. Here the reference signal was obtained from an experiment without an RF pulse. Figure 9(b), shows the resulting experimental data for the $V_1/V_3$ and $V_2$ type vacancies. The experimental data were fitted to the function

$$S_{\mathrm{RF}}(\tau_R) - S_0(\tau_R) = A + B\cos(2\pi\nu_R\tau_R - \phi)e^{-\tau_R/T_2^*}, \quad (2)$$

where $S_{\mathrm{RF}}(\tau_R)$ is the signal measured with an the RF pulse of duration $\tau_R$ and $S_0$ $(\tau_R)$ the reference signal without RF pulse. For $V_1V_3$, we obtained the fit parameters $A = 0.54$, $B = -0.66$, $\phi = 0.06\pi$, $\nu_R = 12.44$ MHz, $T_2^\star$ =99.29 ns and for $V_2$ $A = 0.65$, $B = 0.53$, $\phi = -0.08\pi$ $\nu_R = 8.36$ MHz, $T_2^* = 204.81$ ns.

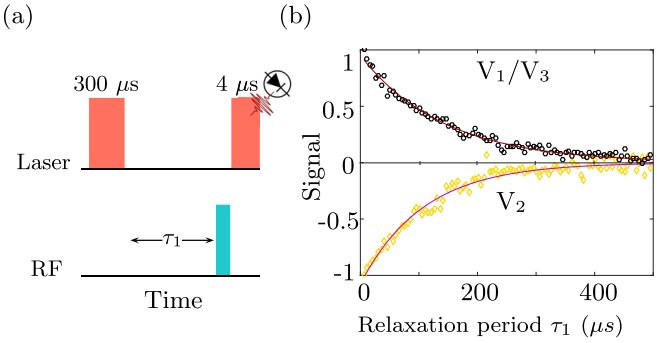


FIG. 10. (a) Pulse sequence used to measure the $T_1$ relaxation. The red and blues rectangles represent the laser and RF pulses. The length of the pulse is written above the pulse. (b) Resulting signal (normalized) as a function of the delay $\tau_1$, measured at room temperature.

## IV. RELAXATION MEASUREMENTS

### A. Population relaxation

Spin-lattice relaxation is the process by which the populations of the spin system relax to the thermal equilibrium state. It is also known as longitudinal relaxation and contributes to the decoherence process. The pulse sequence used to measure the longitudinal relaxation is shown in Fig. 10(a). After the initializing laser pulse the system was allowed to relax for a time $\tau_1$ and then the measuring laser pulse was applied to record the remaining population difference. The result of this experiment was subtracted from a similar experiment where the populations of the levels $|0\rangle$ and$|1\rangle$ were inverted by a $\pi$ pulse applied to the transition between them. Figure 10(b) shows the resulting signals for both vacancy spins as a function of the delay $\tau_1$. The experimental signal was fitted to the function

$$S_\pi(\tau_1) - S_0(\tau_1) = Ae^{-\tau_1/T_1},$$

where $S_\pi(\tau_1)$ and $S_0(\tau_1)$ are the average signal measured during the reference and the main pulse sequence, respectively, for different delays $\tau_1$. From the fit, we obtained the $T_1$ relaxation times $142.1 \pm 3.6$ $\mu$s and $107 \pm 6.6$ $\mu$s for the $V_1/V_3$ and $V_2$ sites, respectively.

### B. Free induction decay

Another important process is the decay of coherence, which can be observed in a free induction decay (FID) measurement. While the free precession of spin coherence can be observed directly in conventional magnetic resonance, here we used the Ramsey scheme [49] where a $\pi/2$ RF pulse converted the coherence into a population difference, which was then read out during the final laser pulse. Figure 11 shows the experimental scheme: After the initialization by the first laser pulse, the first RF pulse generated the coherence, which was then allowed to precess for a time $\tau_f$ before it was read out. We again used the difference between two experiments, where the two RF pulses have a phase difference of $\phi_d = \nu_{\rm det}\tau_f$ and $\pi + \phi_d$, respectively, to suppress unwanted background signals. Figure 11(b), shows the FIDs measured with a detuning frequency of $\nu_{\rm det} = 40$ MHz, together with a

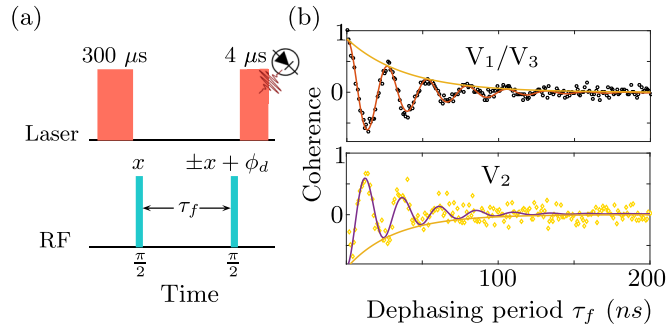


FIG. 11. (a) Pulse sequences for measuring the free-induction decay. The red and blues rectangles represent the laser pulses and RF pulses, respectively. The pulse duration is written above the pulse. (b) FID signals measured for $V_1/V_3$ and $V_2$.

fit to the a function

$$S_{x+\phi_d} - S_{-x+\phi_d} = A\cos(2\pi\nu_{\rm det}\tau_f + \phi)e^{-\tau_f/T_2^*}, \quad (3)$$

where $S_{x+\phi_d}(\tau_f)$ and $S_{-x+\phi_d}(\tau_f)$ are the average PL signals measured with the $\pm x + \phi_d$ detection pulse. The fit parameter $T_2^* = 38$ ns for $V_1/V_3$ and $T_2^* = 31$ ns for $V_2$ at room temperature and in the absence of an external magnetic field.

### C. Spin-echo

The decay of the coherence is due to different types of interactions that are broadly classified as homogeneous vs inhomogeneous. They can be separated by the spin-echo experiment (Hahn-echo) [35]. We will refer to the homogenous decay time of the Hahn echo as $T_2$.

Figure 12(a) shows the pulse sequence for measuring the spin-echo relaxation. After the initializing laser-pulse, we applied a $\pi/2$ RF pulse, which created the coherence that evolved freely for a time $\tau_2/2$. We then applied a refocusing $\pi$ pulse, and a second $\tau_2/2$ delay. The remaining coherence was converted into population by the third RF pulse and read out during the final laser pulse. In this sequence, all RF pulses were applied along the $x$ axis. In the reference signal, the last $\pi/2$ pulse was applied along the $-x$ axis, which changed the sign of the resulting population difference. Subtracting the

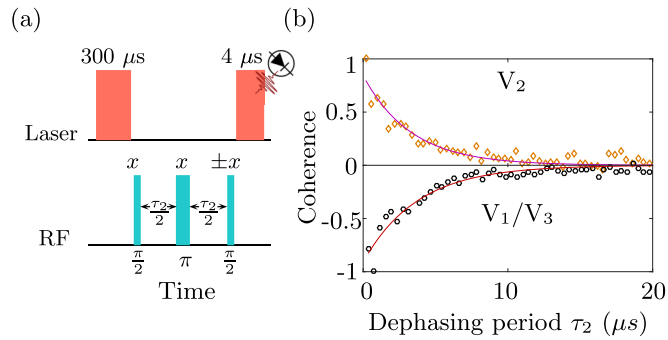


FIG. 12. (a) Pulse sequence used to measure dephasing of the transverse spin components. The red and blue rectangles represent the laser and RF pulses, respectively. The length of the pulses is written above them. (b) Signals measured for $V_1/V_3$ and $V_2$ as a function of the delay $\tau_2$.

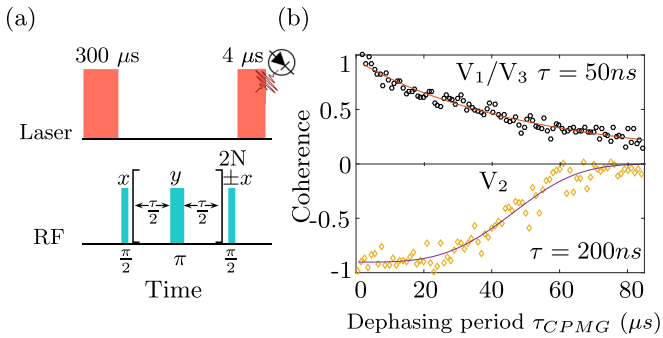


FIG. 13. (a) Pulse sequence for measuring the spin coherence time under multiple refocusing pulses. The red and blues rectangles represent the laser and RF pulses, respectively. (b) Decay of the spin coherence during the multiple echo sequence. The experimental data (circles) are fitted to function (4).

signals from the two experiments thus yielded a background-free measurement of the coherence. Figure 12(b), plots the resulting data as a function of the dephasing period $\tau_2$, together with a fit to an exponential decay

$$S_x - S_{-x} = Ae^{-\tau_2/T_2},$$

where $S_x(\tau_2)$ and $S_{-x}(\tau_2)$ are the signals measured with the $\pm x$ pulse. The resulting values for $T_2$ were $3.73 \pm 0.13$ $\mu$s and $3.31 \pm 0.24$ $\mu$s for the $V_1/V_3$ and $V_2$ centers at room temperature and in the absence of an external magnetic field.

### D. Echo trains

Multiple refocusing pulses can extend the lifetime of the coherence further, compared to the case of a single echo, if the perturbation is not static, but its correlation time is longer than the spacing between the echo pulses [33,36,37]. We therefore measured the coherence time of the centers during a CPMG pulse sequence, as shown in Fig. 13(a). After the initializing laser-pulse, the $\pi/2$ RF pulse created spin coherence. During the subsequent delay, we applied $2N$ refocusing pulses, each with flip angle $\pi$. The final $\pi/2$ pulse converted the coherence back into population which was read out as discussed above. To eliminate background signals, we subtracted the results of the two experiments where the final $\pi/2$ RF pulse rotated the spins around the $\pm x$ axes. The difference between the experimentally observed signals was fitted to the function

$$S_x - S_{-x} = A\, e^{-\left(\tau_{\mathrm{CPMG}}/T_2^{\mathrm{CPMG}}\right)^n}, \qquad (4)$$

where the total evolution period is $\tau_{\mathrm{CPMG}} = 2N\tau + 2N\tau_{\pi\,\mathrm{pulse}}$, $2N$ is number of $\pi$ pulses and $\tau_{\pi\,\mathrm{pulse}}$ is the duration of a $\pi$ pulse, which was 17.5 ns for $V_1/V_3$ and 21 ns for $V_2$. Figure 13(b) shows the experimental data for a pulse spacing of $\tau = 50$ ns for $V_1/V_3$ and $\tau = 200$ ns for $V_2$. The fitted parameters are $T_2^{\mathrm{CPMG}} = 56 \pm 11$ $\mu$s, $n = 0.93$ for $V_1/V_3$ and $T_2^{\mathrm{CPMG}} = 51 \pm 4$ $\mu$s, $n = 3.47$ for $V_2$ at room temperature and in the absence of an external magnetic field.

## V. DISCUSSION AND CONCLUSION

$V_{\mathrm{Si}}^-$ centers in SiC have interesting properties that may become useful in future quantum devices, similar to the NV center in diamond. In this work, we have studied in detail their properties in the 6*H*-SiC polytype. We studied the photoluminescence spectrum as a function of temperature. At low temperature, the ZPLs of the $V_1$, $V_2$, and $V_3$ are quite sharp but broaden with increasing temperature.

These $V_{\mathrm{Si}}^-$ centers can be spin-polarized by optical irradiation, the spin can be manipulated by RF fields and read out optically. In zero field, the ODMR spectrum shows two peaks with opposite amplitudes, one at 28 MHz and the other at 128 MHz. They can be assigned to the $V_1/V_3$ and $V_2$ type $V_{\mathrm{Si}}^-$ [13]. ODMR transitions as a function of the magnetic field parallel to $c$ axis were measured for both $V_{\mathrm{Si}}^-$.

The main emphasis of this work was on the coherence properties of the spins during free precession as well as during the application of refocusing sequences designed to protect the spins against environmental noise. Using a train of echo pulses, we could extend the coherence time of the $V_{\mathrm{Si}}^-$ in the 6*H*-SiC polytype at room temperature up to 50 $\mu$s. Previous experimental room temperature studies on $V_2$ type vacancy in 4*H*-SiC in the absence of external magnetic field reported free evolution time and spin-echo decay times of 190–300 ns and 6–8 $\mu$s, respectively [42,43]. The isotopic composition of the 4*H*-SiC samples used in those studies was natural abundance, i.e., with 4.7 % of $^{29}$Si and 1.1 % of $^{13}$C, both of which have nuclear spins $I = 1/2$. Since the atoms closest to the Si vacancy are all $^{13}$C nuclei, their hyperfine interaction is approximately an order of magnitude stronger than that of the $^{29}$Si nuclei located in the next-nearest neighbor shell consisting of twelve silicon atoms [16,50,51]. The decoherence of the vacancy-spin ensemble is mainly due to dipolar fluctuations of the nuclear spins [50,51] which couple to the electron spin couples by hyperfine interaction [50]. A higher percentage of $^{13}$C therefore reduces the coherence time. We expect that the coherence times can be extended by applying suitable magnetic fields and dynamical decoupling schemes [42,43]. Lowering the temperature will also extend the spin-lattice relaxation time [43]. These possibilities will be explored in upcoming work.

## ACKNOWLEDGMENTS

This work was supported by the Deutsche Forschungsgemeinschaft in the frame of the ICRC TRR 160 (Project No. C7) and by RFBR, Project No. 19-52-12058. SIMS measurements were performed using the Center of Multi-User Equipment “Material Science and Diagnostics for Advanced Technologies" (Ioffe Institute, Russia) facility supported by the Russian Ministry of Science (Agreement ID RFMEFI62119X0021). A.N.A. thanks for supporting the research of the Russian Science Foundation (project No. 19-72-00154).

[1] S. A. Tarasenko, A. V. Poshakinskiy, D. Simin, V. A. Soltamov, E. N. Mokhov, P. G. Baranov, V. Dyakonov, and G. V. Astakhov, Phys. Status Solidi B **255**, 1870101 (2018).

[2] A. L. Falk, B. B. Buckley, G. Calusine, W. F. Koehl, V. V. Dobrovitski, A. Politi, C. A. Zorman, P. X.-L. Feng, and D. D. Awschalom, Nat. Commun. **4**, 1819 (2013).

[3] E. Janzén, A. Gali, P. Carlsson, A. Ga§llstrom, B. Magnusson, and N. Son, Physica B **404**, 4354 (2009).

[4] R. Maboudian, C. Carraro, D. G. Senesky, and C. S. Roper, J. Vac. Sci. Technol. A **31**, 050805 (2013).

[5] B.-S. Song, S. Yamada, T. Asano, and S. Noda, Opt. Expr. **19**, 11084 (2011).

[6] J. Wang, Y. Zhou, X. Zhang, F. Liu, Y. Li, K. Li, Z. Liu, G. Wang, and W. Gao, Phys. Rev. Appl. **7**, 064021 (2017).

[7] M. Widmann, S.-Y. Lee, T. Rendler, N. T. Son, H. Fedder, S. Paik, L.-P. Yang, N. Zhao, S. Yang, I. Booker, A. Denisenko, M. Jamali, S. A. Momenzadeh, I. Gerhardt, T. Ohshima, A. Gali, E. Janzén, and J. Wrachtrup, Nat. Mater. **14**, 164 (2014).

[8] P. G. Baranov, I. V. Il'in, E. N. Mokhov, M. V. Muzafarova, S. B. Orlinskii, and J. Schmidt, J. Exp. Theor. Phys. Lett. **82**, 441 (2005).

[9] N. T. Son, P. N. Hai, M. Wagner, W. M. Chen, A. Ellison, C. Hallin, B. Monemar, and E. Janzén, Semicond. Sci. Technol. **14**, 1141 (1999).

[10] H. Kraus, V. A. Soltamov, D. Riedel, S. Väth, F. Fuchs, A. Sperlich, P. G. Baranov, V. Dyakonov, and G. V. Astakhov, Nat. Phys. **10**, 157 (2013).

[11] P. G. Baranov, A. P. Bundakova, A. A. Soltamova, S. B. Orlinskii, I. V. Borovykh, R. Zondervan, R. Verberk, and J. Schmidt, Phys. Rev. B **83**, 125203 (2011).

[12] F. Fuchs, B. Stender, M. Trupke, D. Simin, J. Pflaum, V. Dyakonov, and G. V. Astakhov, Nat. Commun. **6**, 7578 (2015).

[13] E. Sörman, N. T. Son, W. M. Chen, O. Kordina, C. Hallin, and E. Janzén, Phys. Rev. B **61**, 2613 (2000).

[14] N. Mizuochi, S. Yamasaki, H. Takizawa, N. Morishita, T. Ohshima, H. Itoh, and J. Isoya, Phys. Rev. B **66**, 235202 (2002).

[15] H. J. von Bardeleben, J. L. Cantin, I. Vickridge, and G. Battistig, Phys. Rev. B **62**, 10126 (2000).

[16] M. Wagner, N. Q. Thinh, N. T. Son, W. M. Chen, E. Janzén, P. G. Baranov, E. N. Mokhov, C. Hallin, and J. L. Lindström, Phys. Rev. B **66**, 155214 (2002).

[17] W. E. Carlos, N. Y. Garces, E. R. Glaser, and M. A. Fanton, Phys. Rev. B **74**, 235201 (2006).

[18] S. B. Orlinski, J. Schmidt, E. N. Mokhov, and P. G. Baranov, Phys. Rev. B **67**, 125207 (2003).

[19] N. T. Son, P. Carlsson, J. ul Hassan, E. Janzén, T. Umeda, J. Isoya, A. Gali, M. Bockstedte, N. Morishita, T. Ohshima, and H. Itoh, Phys. Rev. Lett. **96**, 055501 (2006).

[20] D. J. Christle, A. L. Falk, P. Andrich, P. V. Klimov, J. U. Hassan, N. Son, E. Janzén, T. Ohshima, and D. D. Awschalom, Nat. Mater. **14**, 160 (2014).

[21] T. Lingner, S. Greulich-Weber, J.-M. Spaeth, U. Gerstmann, E. Rauls, Z. Hajnal, T. Frauenheim, and H. Overhof, Phys. Rev. B **64**, 245212 (2001).

[22] P. Baranov, V. A. Soltamov, A. A. Soltamova, G. V. Astakhov, and V. D. Dyakonov, *Silicon Carbide and Related Materials 2012*, Materials Science Forum, (Trans Tech, Bäch, Switzerland, 2013) Vol. 740, pp. 425–430.

[23] O. O. Soykal, P. Dev, and S. E. Economou, Phys. Rev. B **93**, 081207(R) (2016).

[24] A. N. Anisimov, V. A. Soltamov, I. D. Breev, R. A. Babunts, E. N. Mokhov, G. V. Astakhov, V. Dyakonov, D. R. Yakovlev, D. Suter, and P. G. Baranov, AIP Advances **8**, 085304 (2018).

[25] D. Riedel, F. Fuchs, H. Kraus, S. Väth, A. Sperlich, V. Dyakonov, A. A. Soltamova, P. G. Baranov, V. A. Ilyin, and G. V. Astakhov, Phys. Rev. Lett. **109**, 226402 (2012).

[26] W. F. Koehl, B. B. Buckley, F. J. Heremans, G. Calusine, and D. D. Awschalom, Nature **479**, 85 (2011).

[27] V. A. Soltamov, A. A. Soltamova, P. G. Baranov, and I. I. Proskuryakov, Phys. Rev. Lett. **108**, 226402 (2012).

[28] D. Simin, V. A. Soltamov, A. V. Poshakinskiy, A. N. Anisimov, R. A. Babunts, D. O. Tolmachev, E. N. Mokhov, M. Trupke, S. A. Tarasenko, A. Sperlich, P. G. Baranov, V. Dyakonov, and G. V. Astakhov, Phys. Rev. X **6**, 031014 (2016).

[29] A. N. Anisimov, D. Simin, V. A. Soltamov, S. P. Lebedev, P. G. Baranov, G. V. Astakhov, and V. Dyakonov, Sci. Rep. **6**, 33301 (2016).

[30] V. A. Soltamov, C. Kasper, A. V. Poshakinskiy, A. N. Anisimov, E. N. Mokhov, A. Sperlich, S. A. Tarasenko, P. G. Baranov, G. V. Astakhov, and V. Dyakonov, Nat. Commun. **10**, 1678 (2019).

[31] D. P. DiVincenzo, Fortschr. Phys. **48**, 771 (2000).

[32] J. Stolze and D. Suter, *Quantum Computing: A Short Course from Theory to Experiment*, 2nd ed. (Wiley-VCH, Berlin, 2008).

[33] D. Suter and G. A. Álvarez, Rev. Mod. Phys. **88**, 041001 (2016).

[34] D. A. Lidar, I. L. Chuang, and K. B. Whaley, Phys. Rev. Lett. **81**, 2594 (1998).

[35] E. Hahn, Phys. Rev. **80**, 580 (1950).

[36] H. Y. Carr and E. M. Purcell, Phys. Rev. **94**, 630 (1954).

[37] S. Meiboom and D. Gill, Rev. Sci. Instrum. **29**, 688 (1958).

[38] A. M. Souza, G. A. Álvarez, and D. Suter, Phys. Rev. Lett. **106**, 240501 (2011).

[39] A. M. Souza, G. A. Álvarez, and D. Suter, Philos. Trans. R. Soc. A **370**, 4748 (2012).

[40] M. Zhong, M. P. Hedges, R. L. Ahlefeldt, J. G. Bartholomew, S. E. Beavan, S. M. Wittig, J. J. Longdell, and M. J. Sellars, Nature **517**, 177 (2015).

[41] J. H. Shim, I. Niemeyer, J. Zhang, and D. Suter, Europhys. Lett. **99**, 40004 (2012).

[42] S. G. Carter, O. O. Soykal, P. Dev, S. E. Economou, and E. R. Glaser, Phys. Rev. B **92**, 161202(R) (2015).

[43] D. Simin, H. Kraus, A. Sperlich, T. Ohshima, G. V. Astakhov, and V. Dyakonov, Phys. Rev. B **95**, 161201(R) (2017).

[44] M. Wagner, B. Magnusson, W. M. Chen, E. Janzén, E. Sörman, C. Hallin, and J. L. Lindström, Phys. Rev. B **62**, 16555 (2000).

[45] T. Biktagirov, W. G. Schmidt, U. Gerstmann, B. Yavkin, S. Orlinskii, P. Baranov, V. Dyakonov, and V. Soltamov, Phys. Rev. B **98**, 195204 (2018).

[46] M. A. Nielsen and I. L. Chuang, *Quantum Computation and Quantum Information* (Cambridge University Press, Cambridge, UK, 2000).

[47] S. P. Depinna and B. C. Cavenett, J. Phys. C **15**, L489 (1982).

[48] L. Langof, E. Ehrenfreund, E. Lifshitz, O. I. Micic, and A. J. Nozik, J. Phys. Chem. B **106**, 1606 (2002).

[49] N. F. Ramsey, Phys. Rev. **78**, 695 (1950).

[50] L.-P. Yang, C. Burk, M. Widmann, S.-Y. Lee, J. Wrachtrup, and N. Zhao, Phys. Rev. B **90**, 241203(R) (2014).

[51] W. M. Witzel, R. de Sousa, and S. Das Sarma, Phys. Rev. B **72**, 161306(R) (2005).